

See discussions, stats, and author profiles for this publication at: <https://www.researchgate.net/publication/224893007>

# Nanopatterning of Electrode Surfaces as a Potential Route to Improve the Energy Density of Electric Double-Layer Capacitors: Insight from Molecular Simulations

ARTICLE *in* JOURNAL OF PHYSICAL CHEMISTRY LETTERS · MARCH 2012

Impact Factor: 7.46 · DOI: 10.1021/jz300253p

---

CITATIONS

30

---

READS

91

## 4 AUTHORS, INCLUDING:



Lidan Xing

South China Normal University

72 PUBLICATIONS 940 CITATIONS

[SEE PROFILE](#)



Jenel Vatamanu

University of Utah

38 PUBLICATIONS 867 CITATIONS

[SEE PROFILE](#)



Dmitry Bedrov

University of Utah

164 PUBLICATIONS 3,155 CITATIONS

[SEE PROFILE](#)

# Nanopatterning of Electrode Surfaces as a Potential Route to Improve the Energy Density of Electric Double-Layer Capacitors: Insight from Molecular Simulations

Lidan Xing,<sup>†,‡</sup> Jenel Vatamanu,<sup>\*,†</sup> Grant D. Smith,<sup>§</sup> and Dmitry Bedrov<sup>†</sup>

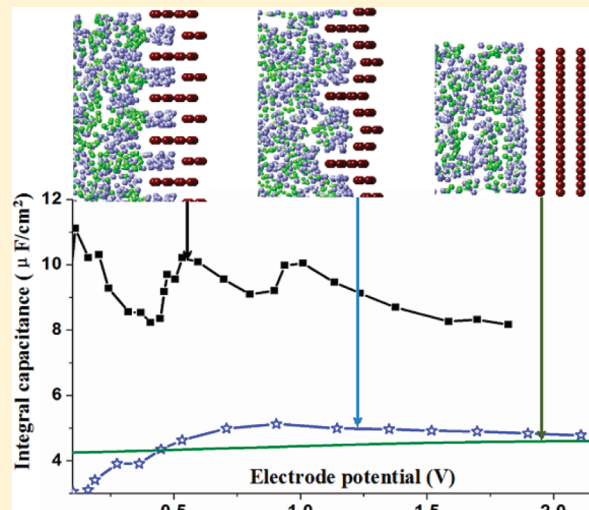
<sup>†</sup>Department of Materials Science and Engineering, University of Utah, 122 South Central Campus Drive, Salt Lake City, Utah 84112, United States

<sup>‡</sup>School of Chemistry and Environment, South China Normal University, Guangzhou 510006, China

<sup>§</sup>Wasatch Molecular Inc., Salt Lake City, Utah 84103, United States

## Supporting Information

**ABSTRACT:** Electrostatic double-layer capacitors (EDLCs) with room-temperature ionic liquids (RTILs) as electrolytes are among the most promising energy storage technologies. Utilizing atomistic molecular dynamics simulations, we demonstrate that the capacitance and energy density stored within the electric double layers (EDLs) formed at the electrode–RTIL electrolyte interface can be significantly improved by tuning the nanopatterning of the electrode surface. Significantly increased values and complex dependence of differential capacitance on applied potential were observed for surface patterns having dimensions similar to the ions' dimensions. Electrode surfaces patterned with rough edges promote ion separation in the EDL at lower potentials and therefore result in increased capacitance. The observed trends, which are not accounted for by the current basic EDL theories, provide a potentially new route for optimizing electrode structure for specific electrolytes.



## SECTION: Energy Conversion and Storage; Energy and Charge Transport

Electrochemical double-layer capacitors (EDLCs) or supercapacitors provide unmatched efficiency and power density in comparison to other energy storage devices. Supercapacitors store energy through the accumulation of counterions (of opposite charge to the electrodes) in a several nanometer wide interfacial layer between an organic electrolyte and high specific surface area electrodes. The absence of Faradic reactions eliminates phase changes in the electrode as well as side reactions (reduction and oxidation of the electrolyte) during the charge/discharge cycles that are problematic in batteries (e.g., lithium ion batteries) that employ organic electrolytes. Supercapacitors can therefore sustain millions of cycles, while batteries survive a few thousand at best. A significant improvement in EDLC performance has been achieved due to recent advances in the understanding of charge storage mechanisms, the development of advanced nanostructured electrode materials,<sup>1–9</sup> and the ability to utilize room-temperature ionic liquids (RTILs) as electrolytes.<sup>10–12</sup> RTILs are in general electrochemically and thermally more stable than conventional organic solvent-based electrolytes, allowing for higher charging voltages at the expense of lower charge-

discharge rates. The wide range of ionic structures available is one of the most appealing aspects of RTILs, providing tremendous potential for the optimization of supercapacitor performance through control of cation and anion size, physicochemical/electrochemical properties, and, perhaps most importantly, interfacial interactions between the electrolyte and the electrodes, which can also be controlled through modification of the electrode surface. In this Letter, we demonstrate, through atomistic molecular dynamics (MD) simulations, that nanopatterning of the electrode surfaces can result in significantly greater stored energy for a given applied potential when structural dimensions of the electrode surface are commensurate with ion dimensions.

The simulated systems consisted of an *N*-methyl-*N*-propylpyrrolidinium bis(fluorosulfonyl)imide [pyr<sub>13</sub>][FSI] ionic liquid confined between two graphite electrodes with the prismatic face exposed toward the electrolyte. The electrode

Received: March 2, 2012

Accepted: April 9, 2012

surface was nanopatterned with parallel grooves, as illustrated in Figure 1. The groove depths are between 5 and 7 Å and

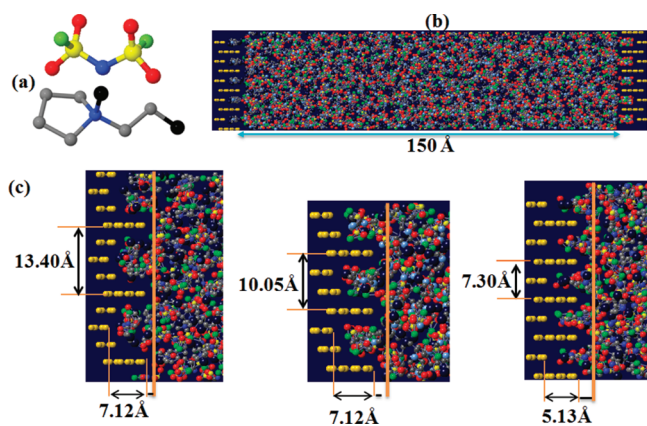


**Figure 1.** (a) The chemical structures of pyr<sub>13</sub> and FSI ions. The O, F, N, and S atoms are represented, respectively, by red, green, blue, and yellow spheres. The CH<sub>3</sub> and CH<sub>2</sub> groups are represented by black and gray spheres, respectively. (b) A snapshot of the simulation cell at a 4.4 V potential between the electrodes. The electrode atoms are represented as gold spheres. (c) Snapshots of the electrode surfaces investigated.

hence can be considered as striations on the surface rather than nanopores. Electrode surfaces with groove widths of 13.4, 10.0, and 7.3 Å (see Figure 1c) were investigated and referred to as S1, S2, and S3, respectively. Note that the groove width for S1 is sufficiently large to fit more than one ion in the lateral direction across the groove, while for S3, the groove is only wide enough to accommodate a single ion (see Supporting Information (SI)).

Figure 2a compares the dependence of the differential capacitance (DC) on the electrode potential for nanopatterned (S1–S3) and flat electrode surfaces. Note that all electrode potentials reported here are relative to the potential of zero charge (PZC). For the system with the widest grooves (S1), a typical camel-shaped DC is observed, having the U-shaped minimum at around 0 V and flanked by two maxima at −0.8 and +0.5 V. Qualitatively, such behavior was explained by the Kornyshev model<sup>13</sup> as arising from steric excluded volume interactions and the specific ionic ordering near flat surfaces. Decreasing the width of the surface patterns to 10.0 Å (S2) results in significantly different behavior of DC. In the potential range where the DC of S1 is U-shaped, the DC of S2 shows a double-peaked bell-shaped dependence on the electrode potential. For the positive electrode, the S2 shows another pronounced peak in DC at +1.7 V that is not observed for S1. Within an electrode potential window of ±2 V (which is of practical interest), the DC values range between 3.3 and 5.6  $\mu\text{F}/\text{cm}^2$  for S1 and between 4.0 and 8.3  $\mu\text{F}/\text{cm}^2$  for S2. The magnitudes of DC observed for the S1 system are in a typical range observed experimentally for similar electrolytes<sup>14–17</sup> on various electrodes and are similar to the values (4.0–5.0  $\mu\text{F}/\text{cm}^2$ ) obtained for this RTIL on atomically flat basal plan graphite,<sup>18</sup> while the DCs for the S2 system are somewhat larger. However, the variation in DC between the main minima and maxima observed for S1 and S2 is noticeably larger than the variations near the flat electrode surface.<sup>18,19</sup> Near flat surfaces and below the saturation potential, the DCs are almost constant,<sup>18–21</sup> while S1 and S2 show up to 50% changes in DCs

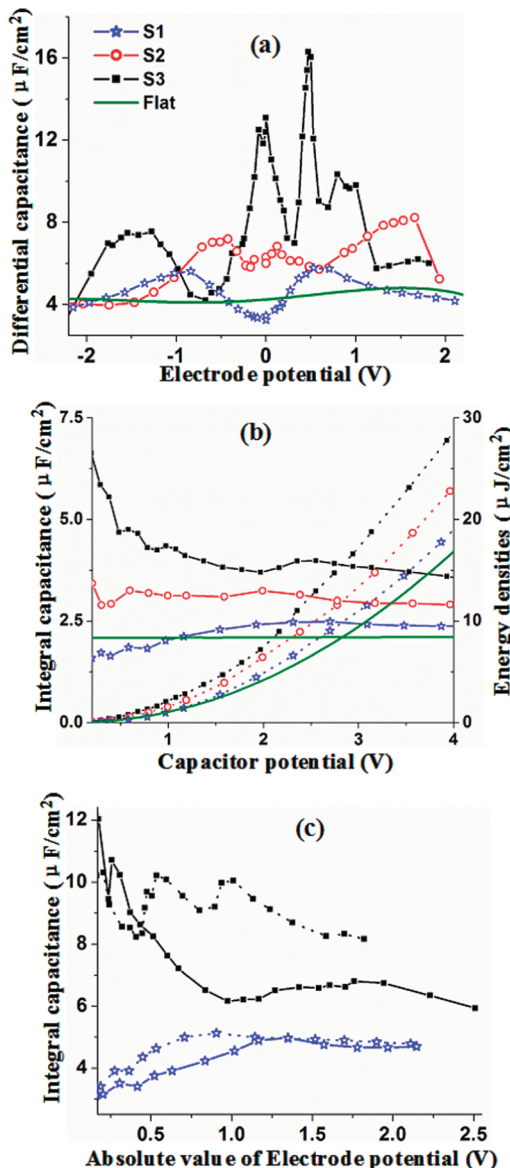


**Figure 2.** (a) The differential capacitance as a function of electrode potential obtained for S1, S2, S3, and flat surfaces. Note that the DC for the flat surface given here for comparison was previously reported by us in ref 18. (b) The integral capacitance (solid lines, left y-axis) and the energy density of the capacitor (dashed lines, right y-axis) as a function of potential difference between electrodes. (c) Integral capacitance of individual electrodes as a function of the absolute value of the electrode potential for systems S1 and S3. Solid lines are for the positive electrode, and dashed lines are for the negative electrode.

(Figure 2a), indicating that the atomic-scale surface corrugation makes DC more sensitive to changes in electrode potential.

As the groove width is further reduced (S3), strikingly different behavior of DC is observed. In the electrode potential range of ±2.0 V, DC for S3 shows surprisingly large variations (up to a factor of 4) ranging between 4.2 and 16.3  $\mu\text{F}/\text{cm}^2$  as well as a complex dependence on the applied potential consisting of four maxima at −1.5, 0.0, +0.5, and +0.8 V and three minima located at −0.8, +0.3, and +0.7 V. Basic EDL theories<sup>13,22</sup> based on electrolyte ordering and excluded volume effects between ions near flat surfaces predict DCs with a single (i.e., bell-shaped) or double (i.e., camel-shaped) peak and at most one minimum near PZC.<sup>13</sup> Clearly, these EDL

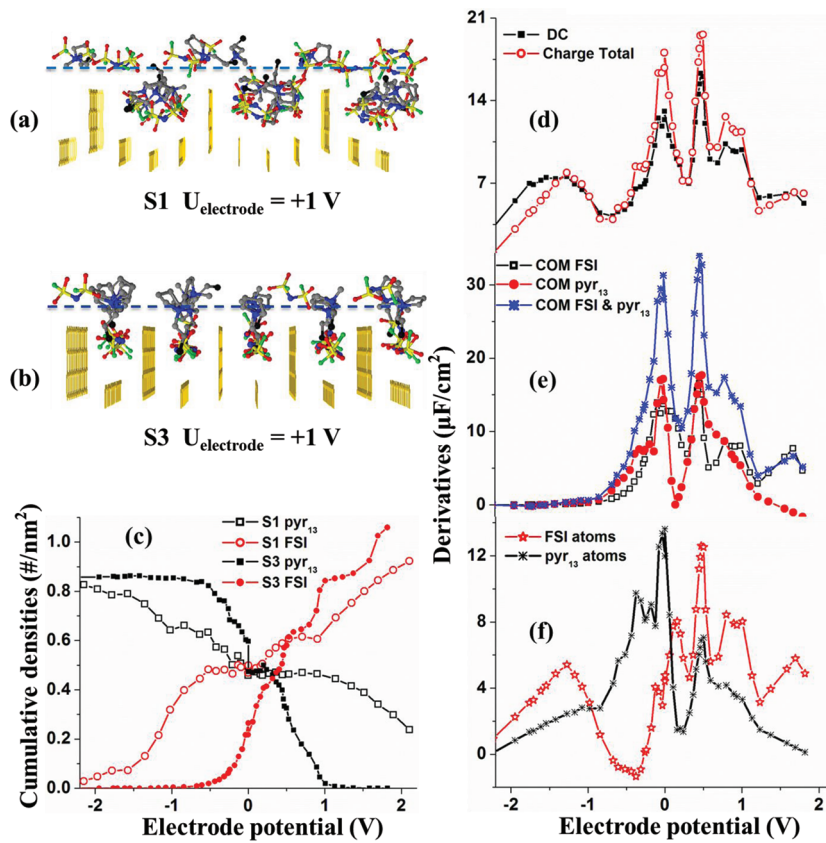


**Figure 3.** (a,b) Snapshots showing the electrolyte structure near positive S1 and S3 surfaces at +1 V, respectively. It is apparent from these snapshots that S3 segregates the ions near the surface to a larger extent than S1. (c) The cumulative densities of the pyr<sub>13</sub> and FSI ions centers-of-mass within the interfacial layer as a function of electrode potential for S1 and S3 surfaces. (d) The differential capacitance and the derivative of the total charge density in the first interfacial layer. (e) The derivative of the cumulative center-of-mass ion densities in the interfacial layer multiplied by the corresponding ion charge. (f) Derivative of the atomic charge density in the interfacial layer computed by taking into account the cumulative density of each atom multiplied by the corresponding partial atomic charge.

models<sup>13,22</sup> cannot account for the complex dependence of DC on the electrode potential observed for the nanopatterned surface S3. The DCs for S3 are systematically and on average significantly larger than the DCs produced by the same electrolyte near the atomically flat (basal) graphite (Figure 2a).

The dependence of the capacitor energy density on the applied potential and surface nanopatterns is shown in Figure 2b. As the groove width decreases, a systematic increase in energy density is observed, with the energy density of S3 being about 1.5–1.8 times larger than of the flat surface. Similarly, the total integral capacitance ( $IC_{capacitor}$ ) of the capacitor as a function of potential, also shown in Figure 2b, is the largest for S3. Interestingly, the differences in energy density and  $IC_{capacitor}$  between S3 and S1 remain surprisingly large at potentials in the 3–4 V range, indicating that surface nanopatterning can be used to tune the energy density of EDLCs even at large potentials. In order to understand the contributions from individual electrodes, in Figure 2c, the integral capacitance of electrodes ( $IC_{electrode}$ ) is shown for S1 and S3. For S1, the  $IC_{electrode}$  is very similar for both electrodes; although, rather small differences are noticeable below  $\pm 1$  V. However, for S3 at potentials above 0.5 V in magnitude, the  $IC_{electrode}$  on the positive electrode is systematically higher (by about 50%) than that on the negative electrode. It is important to point out that on the positive electrode and above +1 V, the  $IC_{electrode}$  of S3 is between 1.7 and 2 times larger than that of S1. Because cations and anions in RTILs typically have quite different architecture,

size, and shape, the observed differences in  $IC_{electrode}$  imply that nanopatterning of each electrode should be optimized individually according to the counterions' structure in order to maximize the capacitance of the respective EDLs.

The observed dependence of DC on the electrode potential was further correlated with electrolyte structuring near the electrode surface. As the electrode charge increases, the electrolyte restructures near the surface, forming density oscillations that diminish in amplitude as the distance from the electrode increases. This results in space charge oscillations extending up to 40 Å from the electrode (see Figure 2 in the SI). The resulting complex EDL structure screens out the applied potential on the electrode, resulting in zero electric field in the electrolyte beyond 40 Å from the electrode. Despite the complex multilayer structure of the EDL, the behavior of DC can be largely understood by examining changes in the density of ions or their individual atoms that occur in a very thin layer (about 6 Å) of the electrolyte located at the interface (see Figure 3a,b). This interfacial layer contains the first peak of the ion center-of-mass density profile and is defined by the position of the first minimum.

Figure 3c compares the cumulative densities of the pyr<sub>13</sub> and FSI centers-of-mass in the interfacial layer as a function of electrode potential for S1 and S3. At relatively low potentials, the accumulation rates of counterions (and depletion of co-ions) on surfaces are much faster (with respect to changes in the potential) for S3 than those for S1. Also, the S3 surface

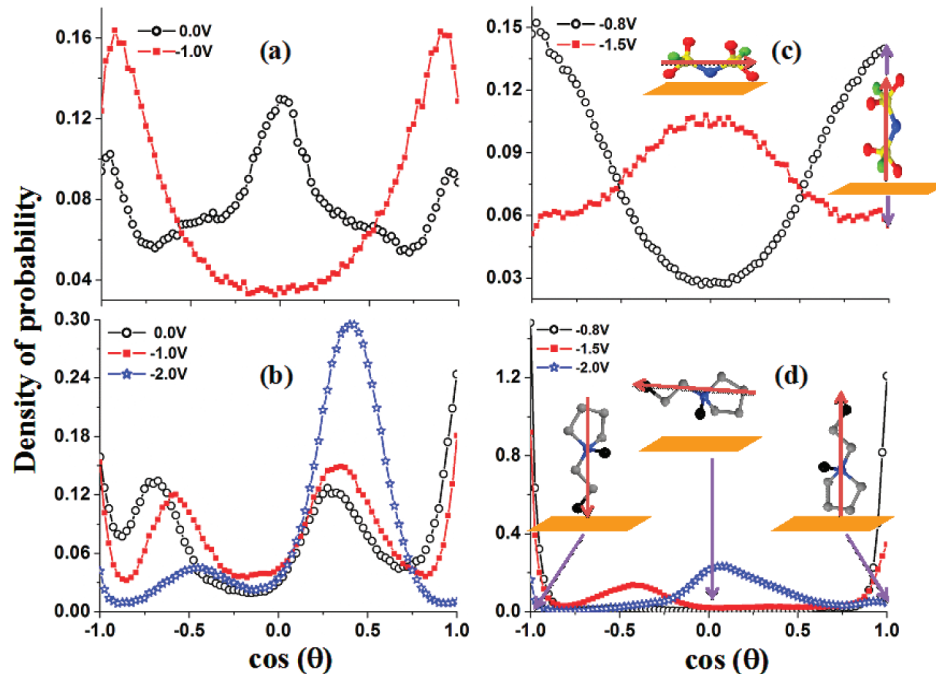


**Figure 4.** Distribution of ion orientations defined by the cosines of the angle  $\theta$  between the “elongated molecular axes” (shown in the panels c and d) and the normal direction to the electrode surface. These distributions are normalized such that  $\int_0^{2\pi} d\varphi \int_{-1}^1 \rho_p d(\cos(\theta)) = 1$ . In the bulk RTIL, these distributions of probability do not depend on  $\cos(\theta)$ , indicating no preference of bulk ions to orient along a particular direction. The upper panels are the orientations for FSI, and the bottom panels are for pyr<sub>13</sub>. The surfaces S1 and S3 are represented in the left and right panels, respectively. The shown potentials correspond to the minima and maxima in DC for the negative electrode.

requires a much smaller potential to reach the surface saturation (flat regions in the density profiles in Figure 3c) and to completely separate the ions in the innermost layer. Such a difference in the response of the interfacial electrolyte layer to the applied potential on S1 and S3 surfaces is in agreement with overall larger capacitances observed for system S3. We also note that the changes in the cumulative density of ions on the S3 surface show a step-like dependence in the potential window between  $-0.5$  and  $+1.5$  V, while for the S1 system, the dependence is more monotonic. The step-like dependence in the cumulative densities of the S3 system is consistent with the enhanced oscillations of DC observed in this potential range for this system.

Next, we provide explanation for the observed features in DC for S3. Figure 3d–f compares the contributions to DC from charge density changes associated with the center-of-mass of the ions as well as individual atoms in the interfacial layer. First, we confirm that the changes in the total charge density in the interfacial electrolyte layer are responsible for the major features observed in DC. Indeed, Figure 3d shows that DC and the derivative of the total charge density in the interfacial layer exhibit remarkably similar dependence on the electrode potential. Next, we examine contributions from cations and anions to DC. Figure 3e shows derivatives of the cumulative center-of-mass ionic densities multiplied with the corresponding ionic charge,  $\sigma_{COM} = \rho_{pyr13}q_{pyr13} + \rho_{FSI}q_{FSI}$ , where  $q_{pyr13} = +1$ ,  $q_{FSI} = -1$ , and  $\rho_{pyr13}$  and  $\rho_{FSI}$  are the center-of-mass densities per unit surface area in the interfacial layer. These derivatives (total and contributions from each ion) have two maxima (at  $0.0$  and  $+0.5$  V) at the same potential as the main maxima in DC and in the derivative of the total charge in the interfacial layer (Figure 3d). However, neither the derivative of the total  $\sigma_{COM}$  nor the derivatives of individual ion

contributions  $\rho_{pyr13}q_{pyr13}$  and  $\rho_{FSI}q_{FSI}$  show any features at potentials below  $-0.5$  V and hence cannot account for the broad peak observed in the DC at around  $-1.5$  V. These derivatives are basically independent of potential in this potential window, indicating that the changes in the interfacial layer charge are not due to changes in ions densities. Also, the values of the  $\sigma_{COM}$  derivative with the potential are noticeably higher than the DC. These two observations point out that there is more to the restructuring of the EDL than just rearrangement of the ion's center-of-mass.

The only way to change charge in the interfacial layer without changing the center-of-mass densities is to reorient ions such that some/different parts of the molecules are outside of the layer while the ion center-of-mass remains in the interfacial layer or change the nature/number of atoms in the interfacial layer from ions whose center-of-mass is outside of the layer. Figure 3f shows contributions to the derivative of the interfacial layer charge arising from various atom types located in the interfacial layer, that is, the derivatives of  $\sum q_{i,pyr13}\rho_{i,pyr13}$  and  $\sum q_{i,FSI}\rho_{i,FSI}$ , where the summation is done over all atoms belonging to pyr<sub>13</sub> or FSI located in the interfacial layer. At low potentials, these derivatives are similar to those computed based on the center-of-mass analysis (compare Figure 3e and f) and are in agreement with DC features observed between  $-0.5$  and  $+2.0$  V. However, in the negative range of potentials ( $-2.5$  to  $-0.5$  V), both contributions show features that were not observed from  $\sigma_{COM}$  analysis. The atom-based contributions to DC from pyr<sub>13</sub> decrease monotonically on the negative electrode, while the contribution from FSI atoms shows a pronounced minimum at  $-0.5$  V followed by a well-defined maximum at  $-1.4$  V. Therefore, the combined effect of these two contributions is responsible for the broad peak observed in DC (Figure 3d) in the negative range of potentials. Taking into

account the values of the cumulative density in the interfacial layer of the O, F, and mass-center of FSI (shown in Figure 3c in the SI) and the constant derivative below  $-0.5$  V for the center-of-mass of FSI (Figure 3e in the SI), we conclude that the fast removal of O and F atoms of the FSI ion on the negative electrode below  $-1$  V generates the maximum of DC at  $-1.5$  V. It is interesting to note that the removal of the co-ion rather than the accumulation of counterions could determine the dominant features of DC at potentials where the surface is populated predominantly by counterions.

The restructuring of the interfacial layer with changing electrode potential discussed above must also be accompanied by a noticeable reorientation of the ions. As shown in Figure 4, there is indeed a significant ion reorientation in the interfacial layer, and it is strongly dependent on the surface structure. For example, the FSI changes its orientation from parallel (but broad) to perpendicular to the S3 surface as the negative potential increases; however, it shows an opposite trend on the negative S1. On weakly charged S3, the pyr<sub>13</sub> orients primarily perpendicular to the surface, while at around  $-2$  V, it reorients parallel to the grooves, maximizing the exposure of positively charged atoms to the surface.

The results and analysis presented above clearly show that the surface nanopatterning can significantly influence DC of the RTIL-based supercapacitor. Two factors appear to contribute to this behavior: (i) steric: within the smallest width patterns, only one row of ions can fit (see the snapshots given in Figure 4 in the SI), and therefore, the number of ionic arrangements is restricted; and (ii) electrostatic: the rough edges of the surface generate large local electric fields around it (see Figure 5 in the SI), which further enhance the affinity for counterions and repulsion for co-ions if the distance between these rough edges is comparable to ionic dimensions. However, the screening of the electrostatic interactions between two innermost counterions decays as  $1/r^2$  along the rough edges rather than exponentially as in a conductive infinitely long pore.<sup>23,24</sup> Therefore, the phenomenon reported here clearly has a different physical origin from the ion behavior inside of confined pores.

In conclusion, our simulations demonstrated that the energy densities in RTIL-based electrostatic capacitors can be noticeably improved by nanopatterning the surface and tuning the surface topography. Surface patterns (or rough edges) having groove widths matching the size of the ions will produce a complex DC dependence on an applied potential consisting of multiple minima and maxima and systematically larger capacitances (and energy densities) due to faster counterion accumulation near the surface and the stronger tendency to segregate ions in the interfacial layer. Importantly, the increased values of capacitance on the nanopatterned surface extend even to a relatively large range of applied potentials ( $3$ – $4$  V). Finally, in this work, we used geometrically well-defined nanopatterning by regularly spaced grooves to illustrate proof of the concept. Technologically achieving such particular patterning of the surface might be costly. However, on the basis of the analysis presented here, we believe that geometric regularity is not essential for the observed trends in DC, and hence, surfaces with random patterning would show similar effects. Generating surfaces with random patterns through grafting some terminal groups or chemically etching the surface will likely be less costly and technologically more viable than precise nanopatterning.

## SIMULATION METHOD

The investigated systems contained 466 ionic pairs of electrolytes confined between two graphite electrodes. The RTIL was modeled using a combined explicit/united atom force field described in ref 18. The potential difference between electrodes was controlled by computing on-the-fly the electrode charges iteratively, subject to the condition of electrostatic energy minimization at the applied electrode potential.<sup>25–27</sup> Such a procedure assumes that the electrode charges redistribute much faster than the electrolyte near the surface and approximates the electrode as a conductor. The equations of motions were integrated with the RESPA scheme<sup>28</sup> as follows; the forces from bonds, bends, and out-of-plane deformations were updated every 0.5 fs, the forces from dihedrals and the short-range (within 7.5 Å) nonbonded interactions were updated every 2.5 fs, and a complete force evaluation was performed every 5 fs. Electrode charges were updated at every 0.25 ps. For each surface, simulations at 16 applied potentials ranging between 0 and 4.4 V have been conducted. For the most interesting system (S3), 10 additional simulations (i.e., 26 dialed potentials total) were generated in order to better resolve the multiple features observed in DC as a function of potential. A simulation time of 50 ns for each potential investigated was sufficient to obtain the convergent statistics. The simulations were conducted at 363 K and atmospheric pressure. The temperature in the system was controlled with the massive Nose–Hoover chains<sup>29</sup> scheme that strictly imposed the energy equipartition, utilizing a similar implementations as that described in ref 30. Electrostatic interactions were computed using the two-dimensional smooth particle mesh Ewald method described in ref 31.

The Poisson potential  $\phi(z)$  across the simulation cell was computed by integrating the Poisson equation,  $\nabla_z[\epsilon_0(\nabla_z\phi(z))] = -\rho(z)$ , where  $z$  is the direction perpendicular to the electrode surface,  $\rho(z)$  is the charge density profile along the  $z$ -direction, and the  $\epsilon_{x0}$  is the vacuum permittivity. The EDL potential ( $U_{EDL}$ ) was computed as the difference between the Poisson potential on the electrode ( $\phi_{electrode}$ ) and the screened Poisson potential in bulk electrolyte ( $\phi_{bulk}$ ),  $U_{EDL} = \phi_{electrode} - \phi_{bulk}$ . The electrode potentials reported here are defined as the EDL potentials relative to the PZC,  $U_{electrode} = U_{EDL} - PZC = \phi_{electrode} - \phi_{bulk} - PZC$ . The PZC was computed as the potential drop within the EDL for uncharged electrodes. PZC values of  $-0.48$ ,  $-0.53$ , and  $-0.45$  V were obtained for systems S1, S2, and S3, respectively, at 363 K. Note that the negative PZCs are consistent with a larger affinity of the uncharged surface for F and O groups of the FSI anion.<sup>18</sup> The DC is defined as the derivative of the electrode surface charge density ( $\sigma$ ) with respect to the EDL potential,  $DC = d\sigma/dU_{EDL}$ .

The DC was obtained by numerically differentiating the dependence of the electrode charge versus the electrode potential obtained from simulations, following the procedure described in ref 32. The integral capacitance of the entire capacitor ( $IC_{capacitor}$ ) is defined as the ratio between the total electrode charge density ( $\sigma$ ) and the applied potential difference between electrodes ( $\Delta U$ ),  $IC_{capacitor} = \sigma/\Delta U$ . The integral capacitance of an individual electrode is defined as the ratio between the total surface charge density ( $\sigma$ ) on the electrode and the EDL potential relative to PZC,  $IC_{electrode} = \sigma/(U_{EDL} - PZC)$ .

The  $IC_{capacitor}$  and  $IC_{electrode}$  are related as  $1/IC_{capacitor} = 1/IC_{electrode(+)} + 1/IC_{electrode(-)}$ . The energy density  $E$  of the

capacitor was obtained as  $E_{\text{capacitor}} = 0.5IC_{\text{capacitor}}\Delta U^2$ . The energy density on the specific electrode was obtained as  $E_{\text{electrode}} = 0.5IC_{\text{electrode}}(U_{\text{EDL}} - \text{PZC})^2$ . Finally, we estimate that our error bars in the density profiles and DCs are less than 1 and 4%, respectively.

## ASSOCIATED CONTENT

### Supporting Information

Additional figures showing ion density profiles, the cumulative density of ions and individual atoms in the first interfacial layer, and lateral distribution of the electrostatic potential near the surface. This material is available free of charge via the Internet at <http://pubs.acs.org>.

## AUTHOR INFORMATION

### Corresponding Author

\*E-mail: jenel.vatamanu@utah.edu.

### Notes

The authors declare no competing financial interest.

## ACKNOWLEDGMENTS

This work is supported by the Department of Energy through DE-AC02-05CH11231 grant on PO No. 6838611 to University of Utah and the ABR DOE program. L.X. acknowledges the China Scholarship Council (CSC) for financial support.

## REFERENCES

- (1) Barbieri, O.; Hahn, M.; Herzog, A.; Kotz, R. Capacitance Limits of High Surface Area Activated Carbons for Double Layer Capacitors. *Carbon* **2005**, *43*, 1303–1310.
- (2) Lu, W.; Hartman, R.; Qu, L.; Dai, L. Nanocomposite Electrodes for High-Performance Supercapacitors. *J. Phys. Chem. Lett.* **2011**, *2*, 655–660.
- (3) Jang, Y.; Ogata, H.; Park, K. C.; Lee, S. H.; Park, J. S.; Jung, Y. C.; Kim, Y. J.; Kim, Y. A.; Endo, M. Exposed Edge Planes of Cup-Stacked Carbon Nanotubes for an Electrochemical Capacitor. *J. Phys. Chem. Lett.* **2010**, *1*, 2099–2103.
- (4) Nakanishi, H.; Grzybowski, B. A. Supercapacitors Based on Metal Electrodes Prepared from Nanoparticle Mixtures at Room Temperature. *J. Phys. Chem. Lett.* **2010**, *1*, 1428–1431.
- (5) Frackowiak, E.; Metenier, K.; Bertagna, V.; Beguin, F. Supercapacitor Electrodes from Multiwalled Carbon Nanotubes. *Appl. Phys. Lett.* **2000**, *77*, 2421–2423.
- (6) Zhang, L. L.; Zhou, R.; Zhao, X. S. Graphene-Based Materials As Supercapacitor Electrodes. *J. Mater. Chem.* **2010**, *20*, 5983–5992.
- (7) Largeot, C.; Portet, C.; Chmiola, J.; Taberna, J. C.; Gogotsi, Y.; Simon, P. Relation between the Ion Size and Pore Size for an Electric Double-Layer Capacitor. *J. Am. Chem. Soc.* **2008**, *130*, 2730–2731.
- (8) Chimola, J.; Yushin, G.; Gogotsi, Y.; Portet, C.; Simon, P.; Taberna, P. Anomalous Increase in Carbon at Pore Size Less than 1 nm. *Science* **2006**, *313*, 1760–1763.
- (9) Simon, P.; Gogotsi, Y. Materials for Electrochemical Capacitors. *Nat. Mater.* **2008**, *7*, 845–854.
- (10) Sato, T.; Masuda, G.; Takagi, K. Electrochemical Properties of Novel Ionic Liquids for Electric Double Layer Capacitor Applications. *Electrochim. Acta* **2004**, *49*, 3603–3611.
- (11) Arbizzani, C.; Biso, M.; Cericola, D.; Lazzari, M.; Soavi, F.; Mastragostino, M. Safe High-Energy Supercapacitors Based on Solvent Free Ionic Liquid Electrolytes Ionic Liquid Electrolytes. *J. Power Sources* **2008**, *185*, 1575–1579.
- (12) Hapiot, P.; Lagrost, C. Electrochemical Reactivity in Room-Temperature Ionic Liquids. *Chem. Rev.* **2008**, *108*, 2238–2264.
- (13) Kornyshev, A. A. Double-Layer in Ionic Liquids: Paradigm Change? *J. Phys. Chem. B* **2007**, *111*, 5545–5557.
- (14) Islam, M. M.; Alam, M. T.; Okijima, T.; Oshaka, T. Electrical Double Layer Structure in Ionic Liquids: An Understanding of the Unusual Capacitance–Potential Curve at a Nonmetallic Electrode. *J. Phys. Chem. C* **2009**, *113*, 3386–3389.
- (15) Alam, M. T.; Islam, M. M.; Okijima, T.; Oshaka, T. Measurements of Differential Capacitance in Room Temperature Ionic Liquid at Mercury, Glassy Carbon and Gold Electrode Interfaces. *Electrochim. Commun.* **2007**, *9*, 2370–2374.
- (16) Lockett, V.; Sedev, R.; Ralston, J.; Horne, M.; Rodopoulos, T. Differential Capacitance of the Electrical Double Layer in Imidazolium-Based Ionic Liquids: Influence of Potential, Cation Size, and Temperature. *J. Phys. Chem. C* **2008**, *112*, 7486–7495.
- (17) Lockett, V.; Horne, M.; Sedev, R.; Rodopoulos, T.; Ralston, J. Differential Capacitance of the Double Layer at the Electrode/Ionic Liquids Interface. *Phys. Chem. Chem. Phys.* **2010**, *12*, 12499–12512.
- (18) Vatamanu, J.; Borodin, O.; Smith, G. D. Molecular Simulations of the Electric Double Layer Structure, Differential Capacitance, and Charging Kinetics for *N*-Methyl-*N*-propylpyrrolidinium Bis-(fluorosulfonyl)imide at Graphite Electrodes. *J. Phys. Chem. B* **2011**, *115*, 3073–3084.
- (19) Vatamanu, J.; Borodin, O.; Smith, G. D. Molecular Insights into the Potential and Temperature Dependences of the Differential Capacitance of a Room-Temperature Ionic Liquid at Graphite Electrodes. *J. Am. Chem. Soc.* **2010**, *132*, 14825–14833.
- (20) Silva, F.; Gomes, C.; Figueiredo, M.; Costa, R.; Martins, A.; Pereira, C. M. The Electrical Double Layer at the [BMIM][PF<sub>6</sub>] Ionic Liquid/Electrode Interface — Effect of Temperature on the Differential Capacitance. *J. Electroanal. Chem.* **2008**, *622*, 153–160.
- (21) Figueiredo, M.; Gomes, C.; Costa, R.; Martins, A.; Pereira, C. M.; Silva, F. Differential Capacity of a Deep Eutectic Solvent Based on Choline Chloride and Glycerol on Solid Electrodes. *Electrochim. Acta* **2009**, *54*, 2630–2634.
- (22) Grahame, D. C. The Electrical Double Layer and the Theory of Electrocapillarity. *Chem. Rev.* **1947**, *41*, 441–501.
- (23) Kondrat, S.; Kornyshev, A. Superionic State in Double-Layer Capacitors with Nanoporous Electrodes. *J. Phys.: Condens. Matter* **2011**, *23*, 022201–5.
- (24) Kondrat, S.; Georgi, N.; Fedorov, M. V.; Kornyshev, A. A. A Superionic State in Nano-Porous Double-Layer Capacitors: Insights from Monte Carlo Simulations. *Phys. Chem. Chem. Phys.* **2011**, *13*, 11359–11366.
- (25) Reed, S. K.; Lanning, O. J.; Madden, P. A. Electrochemical Interface between an Ionic Liquid and a Model Metallic Electrode. *J. Chem. Phys.* **2007**, *126*, 084704–13.
- (26) Vatamanu, J.; Borodin, O.; Smith, G. D. Molecular Dynamics Simulations of Atomically Flat and Nanoporous Electrodes with a Molten Salt Electrolyte. *Phys. Chem. Chem. Phys.* **2010**, *12*, 170–182.
- (27) Vatamanu, J.; Borodin, O.; Smith, G. D. Molecular Dynamics Simulation Studies of the Structure of a Mixed Carbonate/LiPF<sub>6</sub> Electrolyte near Graphite Surface as a Function of Electrode Potential. *J. Phys. Chem. C* **2012**, *116*, 1114–1121.
- (28) Martyna, G. J.; Tuckerman, M. E.; Tobias, D. J.; Klein, M. L. Explicit Reversible Integrators for Extended Systems Dynamics. *Mol. Phys.* **1996**, *87*, 1117–1157.
- (29) Hoover, W. G. Canonical Dynamics: Equilibrium Phase-Space Distributions. *Phys. Rev. A* **1985**, *31*, 1695–1697.
- (30) Vatamanu, J.; Kusalik, P. G. Molecular Dynamics Methodology to Investigate Steady-State Heterogeneous Crystal Growth. *J. Chem. Phys.* **2007**, *126*, 124703–12.
- (31) Kawata, M.; Mikami, M. Rapid Calculation of Two-Dimensional Ewald Summation. *Chem. Phys. Lett.* **2001**, *340*, 157–164.
- (32) Lamperski, S.; Outhwaite, C. W.; Bhuiyan, L. B. The Electric Double-Layer Differential Capacitance at and near Zero Surface Charge for a Restricted Primitive Model Electrolyte. *J. Phys. Chem. B* **2009**, *113*, 8925–8929.